A low temperature solid state reaction to produce hollow $Mn_xFe_{3-x}O_4$ nanoparticles as anode material for lithium ion batteries

Xiaoting Yu[a,b,1], Chaoqi Zhang[a,1], Zhishan Luo[c,d,*], Ting Zhang[e], Junfeng Liu[a], Junshan Li[a], Yong Zuo[a], Jordi Jacas Biendicho[a], Jordi Llorca[f], Jordi Arbiol[e,g], Joan Ramon Morante[a,b], and Andreu Cabot[a,g,*]

a Catalonia Institute for Energy Research - IREC, Sant Adrià de Besòs, Barcelona, 08930, Spain

b Departament of Physics, Universitat de Barcelona, 08028 Barcelona, Spain

c Department of Chemistry, Southern University of Science and Technology (SUSTech), Shenzhen, Guangdong 518055, P. R. China

d SUSTech Academy for Advanced Interdisciplinary Studies, Southern University of Science and Technology (SUSTech), Shenzhen, Guangdong 518055, P. R. China

e Catalan Institute of Nanoscience and Nanotechnology (ICN2), CSIC and BIST, Campus UAB, Bellaterra, 08193 Barcelona, Spain

f Institute of Energy Technologies, Department of Chemical Engineering and Barcelona Research Center in Multiscale Science and Engineering, Universitat Politècnica de Catalunya, EEBE, 08019, Barcelona, Spain

g ICREA, Pg. Lluís Companys 23, 08010 Barcelona, Spain

ABSTRACT

Hollow $Mn_xFe_{3-x}O_4$ nanoparticles (NPs) with an average size of 15 nm were produced from the solid state reaction of Fe_3O_4-Mn_5O_8 heterostructures. Such Fe_3O_4-Mn_5O_8 heterostructures were obtained through the seeded-growth of Mn_5O_8 crystal domains on the surface of hollow Fe_3O_4 NPs produced by the nanoscale Kirkendall effect. Fe_3O_4-Mn_5O_8 heterostructures were subsequently annealed at a relatively low temperature of 500 ℃ to promote the interfusion of Fe and Mn ions without compromising the hollow geometry. Thus produced $Mn_xFe_{3-x}O_4$ nanostructures were tested as anode material in lithium-ion batteries. $Mn_xFe_{3-x}O_4$-based anodes exhibited high energy storage capacities and high-rate capabilities with 1054 mAh g^{-1} at 0.1 A g^{-1} and 369 mAh g^{-1} at 5 A g^{-1}. Additionally, electrodes based on hollow $Mn_xFe_{3-x}O_4$ NPs demonstrated long cycling stability, with capacities up to 887 mAh g^{-1} at 0.3 A g^{-1} after 450 cycles, which translated into a 118% capacity change with respect to the initial cycles. The excellent performance of hollow $Mn_xFe_{3-x}O_4$ NPs as anode material in Li-ion batteries was associated to their proper crystal structure and composition, which provided a high electrical conductivity, and to their small size and hollow geometry, which provided fast kinetics and improved structural stability. Additionally, the presence of carbonized ligands

effectively improved the utilization rate of active materials, facilitated the transportation of electrons and Li^+ ions, and prevented the structural collapse in long term cycling.

Keywords: Ferrite, lithium ion battery, Kirkendall effect, hollow nanoparticle

INTRODUCTION

Mixed metal oxides play fundamental roles in numerous energy conversion and storage technologies, including batteries, fuel cells and photovoltaics, to cite a few. Usually, mixed metal oxides provide higher electrical conductivities and defect densities, richer redox chemistries and additional degrees of freedom to optimize functional properties.[1-2] In this last direction, tuning of the metal ratios allows adjusting lattice parameters, energy band structures, catalytic properties and charge carrier concentrations, among other.

In numerous technological applications, e.g. those involving interaction with a gas or liquid media, an essential step toward performance optimization is to maximize the surface area. This is particularly true in LIBs, which require electrode materials with high surface areas not only to maximize interaction with the electrolyte to enable high lithiation and delithiation rates but also to accommodate the very high volume changes associated with these processes. However, the synthesis of mixed metal oxides with highly porous structures and/or small nanocrystallite dimensions is extremely challenging. At industrial production scales, mixed metal oxides are generally produced through solid state synthesis methods, which typically require long reaction times and temperatures due to the limited ionic diffusion distances. Such severe synthesis conditions not only increase the cost of the product, but also results in materials with large grains and low surface areas.[3]

Mixed spinels and specifically spinel ferrites are a particularly appealing class of mixed metal oxides. Among them, $MnFe_2O_4$ is especially interesting as it is composed of abundant, low-cost and non-toxic elements, and it provides several remarkable functional properties, including a high theoretical capacity as anode material in Li-ion batteries (LIBs)[4-5] and sodium-ion batteries.[6] Actually, spinel Fe_3O_4 and Mn_3O_4 have been also demonstrated as very competitive alternative compounds to traditional anode materials in LIBs.[7-8] However, such elemental oxides are typically characterized by relatively poor cycling stabilities. This limitation is accentuated by their low electrical conductivity, especially at high current densities.[9-10] To mitigate this drawback, the most effective strategy consist in reducing the crystal domain dimensions to the nanoscale and to mix these nanodomains with highly conductive carbon materials. Ideally, the oxide crystal domains should be in the 10 nm size

range and they should additionally present a proper geometry to accommodate the large volume expansion/contraction associated with lithium intercalation.

In this work, we detail a strategy to produce hollow mixed oxide nanoparticles (NPs) from the low temperature solid state reaction of the constituent oxides. To minimize the required ion diffusion distances and thus the necessary reaction temperature, the two oxides were pre-assembled within heterostructured hollow NPs. In particular, we report on the synthesis of hollow $Mn_xFe_{3-x}O_4$ NPs from the solid state reaction of the Fe_3O_4-Mn_5O_8 heterostructures obtained through the epitaxial growth of a single Mn_5O_8 nanodomain on the surface of each hollow Fe_3O_4 NPs. These hollow $Mn_xFe_{3-x}O_4$ NPs are tested here as anode material in LIBs.

EXPERIMENTAL

Chemicals. Iron pentacarbonyl ($Fe(CO)_5$, 99.99%), manganese(II) perchlorate hydrate ($Mn(ClO_4)_2{\cdot}6H_2O$, 99%), xylene (≥98.5%), oleylamine (OAm, >80%), oleic acid (OAc, 90%) and 1-octadecene (ODE, 90%) were purchased from Sigma-Aldrich. Carbon black (99%), polyvinilidene difluoride (PVDF) and dimethyl carbonate (DMC, 99%) were purchased from Alfa Aesar. N-methyl-2- pyrrolidinone (NMP, 99.5%), $LiPF_6$ (98%) and ethylene carbonate (EC, 99%) were purchased from ACROS Organics. Toluene, hexane, chloroform, acetone and ethanol were of analytical grade and obtained from various sources. Milli-Q water was supplied by the PURELAB flex from ELGA. All chemicals were used as received without further purification.

Hollow Fe_3O_4 NPs. Hollow Fe_3O_4 NPs were prepared following a reported procedure, but introducing slight modifications.[11] 10 mL of ODE and 112 μL of OAm were mixed in a 25 mL three-neck flask and degassed under magnetic stirring for 1h at 80 °C. Then, temperature was raised to 180 °C under argon. At this temperature, a precursor solution containing 0.4 ml of $Fe(CO)_5$ in 1.6 ml of ODE was injected rapidly. After 20 min of reaction, an air flow (100 ml/min) was introduced through the solution for 10 min. Afterward, the reaction was cooled down to room temperature. Fe_3O_4 NPs were collected by adding 20 mL of acetone and centrifuging at 8000 rpm for 10 min. NPs were redispersed in 5 mL of chloroform under sonication and washed at least twice with acetone as anti-solvent and chloroform as solvent.

Fe_3O_4-Mn_5O_8 NPs. 20 mg of as-synthesized Fe_3O_4 NPs was mixed with 5 mL of xylene, 0.41 mL of OAm and 80 μl of OAc. Then, the mixture was heated at 80 °C and stirred for 30 min. At this temperature, 1 mL of an aqueous solution containing 0.2 mmol $Mn(ClO_4)_2$ was injected rapidly. The mixture was allowed to react for 1h at 80 °C and then it was cooled down to room temperature. NPs were collected by adding 10 mL of acetone and centrifuging

at 3000 rpm for 3 min. NPs were redispersed in 5 mL of chloroform under sonication and washed at least twice with acetone as anti-solvent and chloroform as solvent.

Hollow $Mn_xFe_{3-x}O_4$ NPs. As-obtained Fe_3O_4-Mn_5O_8 NPs were heated at a rate of 5 °C/min up to 500 °C under an Ar flow for 2h to force the solid state reaction between Fe_3O_4 and Mn_5O_8 to $Mn_xFe_{3-x}O_4$ and at the same time carbonize the organic ligands attached to the NC surface.[12-13]

Solid Fe_3O_4 NPs. Fe_3O_4 NPs were prepared similarly to a reported procedure.[14] 10 mL of ODE and 2 mL of OAc were mixed in a 25 mL three-neck flask and degassed under magnetic stirring for 1h at 80 °C. Then the temperature was raised to 180 °C under an argon blanket. A precursor solution of 0.4 ml of $Fe(CO)_5$ dissolved in 1.6 ml of ODE was injected rapidly. The temperature was increased to 300 °C and kept for 20 min. Then the reaction was cooled down to room temperature. NPs were collected by adding 20 mL of acetone and centrifuging at 8000 rpm for 10 min.

Mn_3O_4 NPs. Mn_3O_4 NPs were prepared following a reported procedure.[15] A mixture of 5 mL of xylene, 0.41 mL of OAm and 80 μl of OAc was heated at 80 °C and stirred for 30 min. Then, 1 ml aqueous solution containing 0.2 mmol $Mn(ClO_4)_2$ was injected rapidly. The reaction was maintained at 80 °C for 1h and then cooled down to room temperature. NPs were collected by adding 10 mL of acetone and centrifuging at 3000 rpm for 3 min. The precipitate was redispersed in 5 mL of chloroform under sonication and washed at least twice.

Structural and chemical characterization. Size and shape of the NPs were examined by transmission electron microscopy (TEM) using a ZEISS LIBRA 120, operating at 120 kV. High resolution transmission electron microscopy (HRTEM) and scanning transmission electron microscopy (STEM) images were obtained using a FEI Tecnai F20 field-emission gun microscope operated at 200 kV with an embedded Gatan image filter for electron energy loss spectroscopy (EELS) analyses. Images were analyzed by means of Gatan Digital Micrograph software. Scanning electron microscopy (SEM) analyses were done in a ZEISS Auriga microscope with an energy dispersive X-ray spectroscopy (EDS) detector operating at 20 kV that allowed studying the NP composition. Powder X-ray diffraction (XRD) patterns were collected directly from the as-synthesized NPs dropped on Si (501) substrate on a Bruker AXS D8 Advance X-ray diffractometer with Ni-filtered (2 μm thickness) Cu Kα radiation (λ = 1.5406 Å) operating at 40 kV and 40 mA. A LynxEye linear position-sensitive detector was used in reflection geometry. X-ray photoelectron spectroscopy (XPS) was performed on a SPECS system equipped with an Al anode XR50 source operating at 150 W and a Phoibos 150 MCD-9 detector. The pressure in the analysis chamber was always below 10^{-7} Pa. The area

analyzed was about 2 mm × 2 mm. The pass energy of the hemispherical analyzer was set at 25 eV and the energy step was set at 0.1 eV. Data processing was performed with the CasaXPS program (Casa Software Ltd., UK). Binding energy values were centered using the C 1s peak at 284.8 eV. Thermogravimetric analyses (TGA) were carried out using a PerkinElmer Diamond TG/DTA instrument. Samples were measured in air from ambient temperature to 500 °C at the heating rate of 5 °C/min. Nitrogen adsorption−desorption events were performed on a BEL-Mini adsorption analyzer.

Electrochemical Measurements. Working electrodes were prepared by doctor blading. Homogeneous slurries were prepared by mixing 80 wt% active materials, 10 wt% carbon black, and 10 wt% PVDF in NMP. The slurry was uniformly coated on copper foil and dried at 80 °C under vacuum overnight. The active material mass loading of each electrode was around 0.8-1.0 mg cm^{-2}. LIBs were assembled in CR 2032 coin cells within an argon-filled glovebox with a lithium metal counter electrode and a polypropylene Celgard 2400 membrane as the separator. The electrolyte consisted of 1 M $LiPF_6$ dissolved in a solution of EC and DMC (v/v=1:1). The cells were galvanostatically cycled within a voltage range of 0.01-3 V using a Neware BTS4008 battery tester at different current densities. Cyclic voltammetry (CV) measurements were performed on a battery tester BCS-810 from Bio-Logic. Electrochemical impedance spectroscopy (EIS) tests were performed using a sinusoidal voltage with amplitude of 5 mV in the frequency range 100 kHz to 10 mHz. All electrochemical measurements were carried out at room temperature.

RESULTS AND DISCUSSION

Fe_3O_4-Mn_xO_y heterostructured NPs were synthesized through a two-step process. First, Fe_3O_4 hollow NPs were produced through the nanoscale Kirkendall effect by in situ oxidizing colloidal Fe NPs obtained from the decomposition of $Fe(CO)_5$.[11] In a second step, hollow Fe_3O_4 NPs were used as seeds for the epitaxial growth of Mn_xO_y crystals upon injection of a manganese(II) perchlorate aqueous solution (see experimental section for details). TEM micrographs of Fe_3O_4-Mn_xO_y heterostructured NPs obtained following this procedure showed the initial hollow Fe_3O_4 NPs to have an average diameter of 15.5 ± 1 nm and the grown Mn_xO_y crystal domains to have an average size of around 9 ± 1 nm (Figures 1 and S1). Remarkably, in most cases only one Mn_xO_y nanocrystal, which adopted an octahedral geometry, was grown on the surface of each Fe_3O_4 NP. No independent Mn_xO_y nanocrystals could be observed. These results pointed out to a preferential heterogeneous over homogeneous nucleation of Mn_xO_y crystals over Fe_3O_4, a favored crystal growth over

nucleation of new Mn_xO_y domains and to a relatively high interface energy between Fe_3O_4 and Mn_xO_y that favored the formation of a unique Mn_xO_y crystal domain and not a shell at the surface of each Fe_3O_4 NP.

XRD patterns obtained from Fe_3O_4-Mn_xO_y NPs displayed only the peaks corresponding to the magnetite Fe_3O_4 crystal structure (JCPDS 01-088-0315, Figure S2). XRD peaks associated to any of the Mn_xO_y crystal phases could not be distinguished.

HRTEM micrographs showed the heterostructured NPs to have a good crystallinity and to contain multiple crystal domains (Figures 1c and S3). The polycrystalline Fe_3O_4 shell displayed a crystal structure that matched with a cubic Fe_3O_4 (space group Fd3-m) phase, with a=b=c=8.3799 Å. The crystal domain grown from the Fe_3O_4 NP surface matched a Mn_5O_8 monoclinic phase (space group=C2/m) with a=10.3470 Å, b=5.7240 Å and c= 4.8520Å.

Figure 1d shows a STEM micrograph and the corresponding EELS chemical composition maps for Fe, Mn and O of several Fe_3O_4-Mn_5O_8 NPs. Additional compositional maps and the individual oxidation state maps for Mn and Fe obtained from the EELS core loss spectra at the Mn $L_{2,3}$ and Fe $L_{2,3}$ edges can be found on the supporting information (Figures S4-S7). From these chemical maps, it became evident that oxygen was homogeneously distributed throughout the heterostructures. On the other hand, iron was present just at the quasi-spherical hollow NPs and Mn was only present in the octahedral crystal domains grown at the surface of the hollow NPs, confirming the growth of the manganese oxide as a separate phase. A compositional line profile for Fe, Mn and O recorded along the red arrow in the STEM image (Figure 1d) met this conclusion well (Figure 1e).

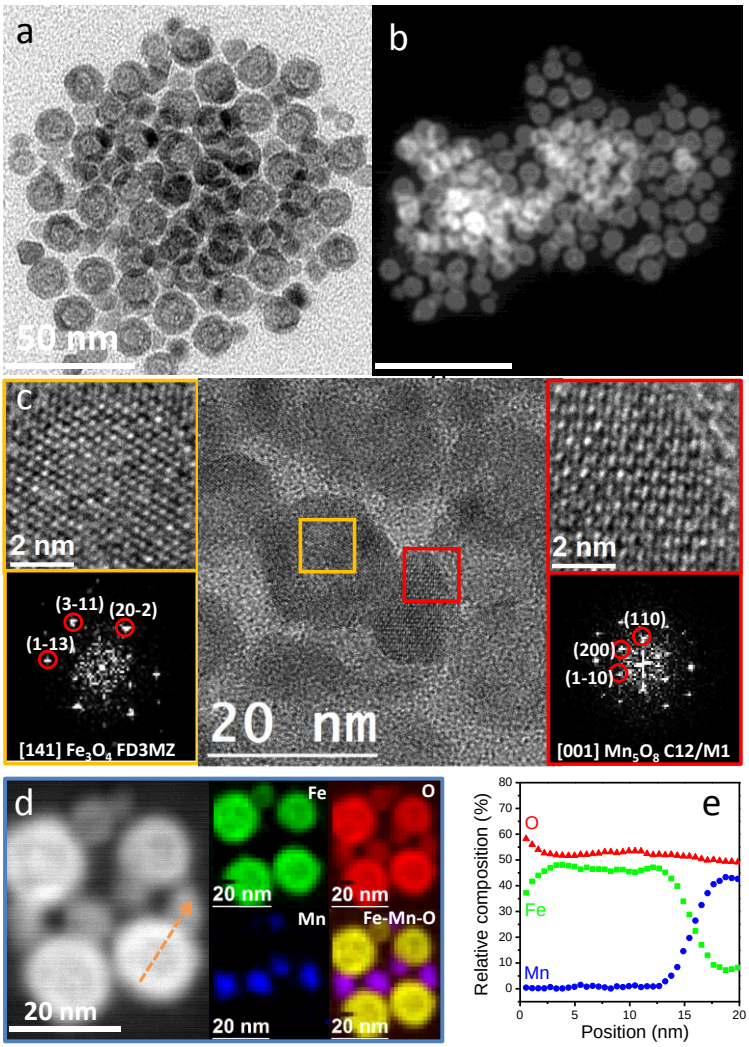

Figure 1. a) TEM and b) SEM micrograph of Fe_3O_4-Mn_5O_8 heterostructured NPs. c) HRTEM micrograph of Fe_3O_4-Mn_5O_8 NPs (middle) and detail of the squared regions and their corresponding power spectrum for the hollow NP (left) and for the faceted domain grown on its surface (right). The crystal in the orange square matched a cubic Fe_3O_4 (space group Fd3-m) phase, with a=b=c=8.3799 Å. The Fe_3O_4 lattice fringe distances were measured to be 0.254 nm, 0.251 nm and 0.296 nm, at 50.42° and 114.85°, which was interpreted as the cubic Fe_3O_4 phase visualized along its [141] zone axis. The magnified detail in the red squared region and its corresponding power spectrum revealed the selected crystal structure to agree with the Mn_5O_8 monoclinic phase (space group=C2/m) with a=10.3470 Å, b=5.7240 Å and c= 4.8520Å. The Mn_5O_8 lattice fringe distances were measured to be 0.506 nm, 0.498 nm and 0.512 nm, at 62.08° and 121.79°, which was interpreted as the monoclinic Mn_5O_8 phase visualized along its [001] zone axis. d) STEM micrograph and EELS chemical composition maps: individual Fe $L_{2,3}$-edges at 708 eV (green), Mn $L_{2,3}$-edges at 640 eV (blue), O K-edge at 532 eV (red) and their composite (Fe-Mn-O). e) Compositional line profile for Fe, Mn and O recorded along the red arrow in image (d).

In a previous report, Lee *et al.* demonstrated that on the surface of solid Fe_3O_4 NPs the number of MnO crystal domains grown at 320 °C from a manganese acetate solution in the presence of OAc depended on the size of the Fe_3O_4 NP.[16] According to Lee et al., 5 nm Fe_3O_4 seeds resulted in the formation of core-shell Fe_3O_4@MnO heterostructures, 11 nm Fe_3O_4 seeds lead to the formation of Fe_3O_4-MnO dumbbells with a unique MnO domain per particle, and 21 nm Fe_3O_4 seeds resulted in Fe_3O_4-MnO heterostructures with multiple MnO crystal domains. The formation of core-shell structures was explained with the very large surface chemical potential of the small Fe_3O_4 NPs used as seeds with a high radius of curvature. Besides, the formation of one or multiple MnO domains on larger crystals was related to the presence of particular sites that facilitated nucleation and/or allowed better accommodation of an interface. At a similarly high temperature, using Mn-oleate as precursor and 11 nm solid Fe_3O_4 seeds, Li *et al.* reported the formation of Fe_3O_4-MnO heterostructures with not well defined sizes and an unclear phase distribution.[17] Recently, Mayence *et al.* reported the formation of Fe_3O_4-MnO heterostructures, mainly dimers, at 250 °C using solid iron oxide nanocubes and manganese(II) acetate as precursor.[18] They evidenced the solvent to strongly influence the heterostructure formation. Mayence *et al.* observed the preferential growth of Mn_3O_4 on the edges of the Fe_3O_4 nanocubes owing to the existence of a common crystallographic orientation and a lattice mismatch of 5%. More recently, Jiang and Peng reported the facet-selective epitaxial growth of Mn_3O_4 nanodomains on Fe_3O_4 at temperatures around 200 °C using manganese decanoate as precursor.[19] They found out the temperature to have a key role in the selective growth of Mn_3O_4 on the vertexes or the top face of solid Fe_3O_4 nanoprisms and explained these results in terms of the site reactivity and the nature of the surfactant bonding to the Fe_3O_4 surface.

Our work differentiates from previous ones in that we used hollow instead of solid Fe_3O_4 NPs as seeds, manganese(II) perchlorate as manganese precursor and relatively low synthesis temperatures, down to 80 °C. To better understand the mechanism of formation of Fe_3O_4-Mn_5O_8 heterostructured NPs in the conditions used in the present work, aliquots from the reaction mixture containing the Fe_3O_4 NPs seeds and the Mn_5O_8 precursor were collected and analyzed by TEM (Figure S8). Small Mn_5O_8 crystal domains were already found on the Fe_3O_4 shell after 15 min of reaction. From this very initial stage of formation of the Mn_5O_8 crystal domains only one Mn_5O_8 crystal per Fe_3O_4 NP was observed. The size of the Mn_5O_8 crystal increased with time until 60 min of reaction. When larger excess amounts of manganese(II) perchlorate were injected into the Fe_3O_4 NPs solution, isolated small Mn_5O_8 NPs could be observed (Figure S9).

In the synthesis conditions used in this work, the manganese precursor selection was fundamental. The use of manganese(II) acetate for instance did not result in heterostructured NPs but on the growth of independent Mn_xO_y NPs (Figure S10). On the other hand, the use of solid Fe_3O_4 NPs instead of hollow Fe_3O_4 NPs resulted in a much larger dispersion of the types of nanostructure formed, with a larger number of Fe_3O_4 NPs containing none or multiple Mn_xO_y domains and a larger number of isolated Mn_xO_y NPs (Figure S11). We hypothesize that compared with solid Fe_3O_4 NPs, the defective and thin shell of the hollow Fe_3O_4 NPs provided a larger number of sites for Mn_5O_8 nucleation and helped to accommodate the stress caused by the Mn_5O_8 growth, resulting in rapid nucleation and growth of Mn_5O_8 crystals that minimized interface energy by reducing the Fe_3O_4-Mn_5O_8 contact area.

Fe_3O_4-Mn_5O_8 heterostructured NPs were annealed at 500 °C under an argon atmosphere to force the solid state reaction between Fe_3O_4 and Mn_5O_8 domains. In the same process, surface organic ligands were carbonized.[12-13] This process did not significantly change the size and morphology of the NPs, although the interior cavity of the hollow NPs, which initially contained some residual material, i.e. displayed a yolk-shell type nanostructure, became fully empty through the diffusion of the internal iron oxide toward the oxide shell. Nevertheless, the hollow geometry of the NPs and the presence of an additional crystal domain on its surface were maintained after the sintering step (Figure 2).

Figure 2c shows a HAADF-STEM micrograph and the corresponding EELS chemical composition maps from several annealed NPs (additional images can be found in Figures S12-S14). On the contrary to the former Fe_3O_4-Mn_5O_8 heterostructured NPs, EELS analysis of the annealed material displayed a homogeneous distribution of Fe, Mn and O throughout the whole NP. HRTEM micrographs and power spectrum analyses of the annealed NPs revealed their crystal structure to match a $MnFe_2O_4$ cubic phase (space group =Fd3m) with a=b=c=8.4190 Å. Additionally, XRD analysis confirmed the $MnFe_2O_4$ crystal phase of the annealed NPs and displayed no additional crystalline phase (Figure S16). EDS analysis showed the ratio of Mn to Fe to be Fe/Mn~2.0 $\pm$ 0.2 when using a nominal Fe/Mn=1.3, denoting the incomplete reaction of the Mn precursor during the Fe_3O_4-Mn_5O_8 seeded-growth. This ratio changed with the nominal amount of Mn precursor added.

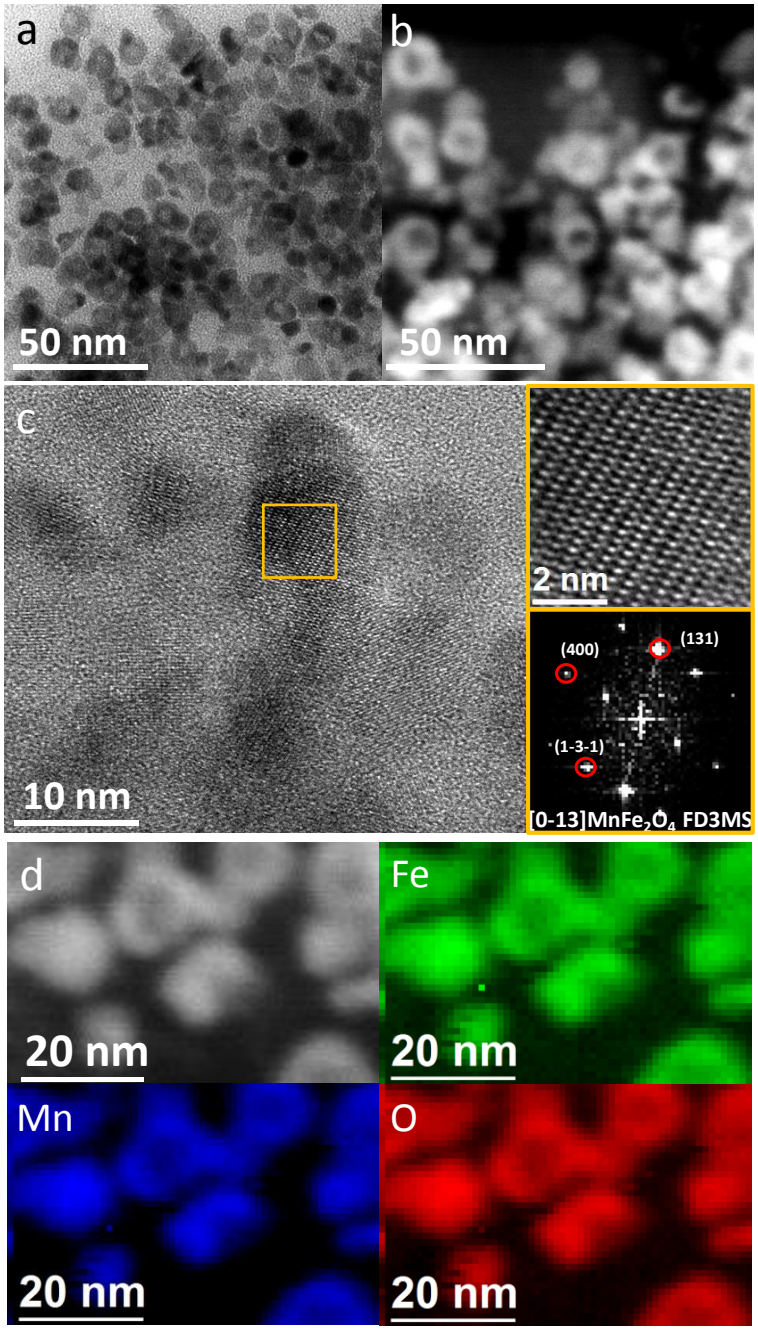

Figure 2. $Mn_xFe_{3-x}O_4$ NPs obtained after the annealing process at 500 °C: a) TEM micrograph b) STEM micrograph. c) HRTEM micrograph, detail of the squared region and corresponding power spectrum. Crystal lattice fringe distances were measured to be 0.255 nm, 0.209 nm and 0.255 nm, at 73.43° and 146.98°, which could be interpreted as the cubic $MnFe_2O_4$ phase, visualized along its [0-13] zone axis. d) STEM micrograph of $Mn_xFe_{3-x}O_4$ NPs and the corresponding EELS chemical composition maps: individual Fe $L_{2,3}$-edges at 708 eV (green), O K-edge at 532 eV (red) and Mn $L_{2,3}$-edges at 640 eV (blue).

XPS analysis results were consistent with the formation of a $MnFe_2O_4$ phase (Figure S15). The Fe 2p spectrum (Figure S15a) depicted the characteristic doublet of Fe^{3+} at 724.7 eV (Fe $2p_{1/2}$) and 711.4 eV (Fe $2p_{3/2}$). The satellite peak at 719.5 eV also pointed out at the presence of Fe^{3+}.[20-21] The Mn 2p spectrum displayed peaks at 653.3 eV (Mn $2p_{1/2}$) and 641.7 eV (Mn $2p_{3/2}$), which we assigned to the presence of Mn^{2+} (Figure S15b).[21-22]

These results unequivocally demonstrated the low temperature (500 °C) solid state reaction between Fe_3O_4 and Mn_5O_8 domains within Fe_3O_4-Mn_5O_8 heterostructured NPs to result in the formation of hollow $Mn_xFe_{3-x}O_4$ NPs through the inter-diffusion of Mn and Fe during the annealing process. Notice that ions of both elements diffused throughout the two materials, as both the initial Fe_3O_4 hollow particle and the initial Mn_5O_8 domain changed composition toward a mixed $Mn_xFe_{3-x}O_4$ phase. The relatively low temperature of the process sufficed to completely react the two crystal domains due to their small size and close proximity. To limit the reaction temperature to a relatively low value was also essential to maintain the initial hollow geometry of the Fe_3O_4 NP.

Thermogravimetric analysis (TGA) in air of the $Mn_xFe_{3-x}O_4$ NPs showed the final carbon content to be ca. 9% (Figure S17a). Additionally, N_2 adsorption isotherms obtained on the $Mn_xFe_{3-x}O_4$ NPs showed clear hysteresis loops and a pore-size-distribution consistent with the mesoporous structures of hollow $Mn_xFe_{3-x}O_4$ NPs (Figure S17b).

Hollow $Mn_xFe_{3-x}O_4$ NPs were used as anode material for LIBs. As a reference, we also prepared electrodes based on Mn_3O_4 NPs and electrodes based on Fe_3O_4 NPs, both materials were also annealed at 500 °C (see experimental section for details on the synthesis of the reference materials and on the electrode and LIB preparation and Figures S18 and S19). To evaluate the lithium storage behavior and explore the relationship between the structure and properties, first cyclic voltammetry (CV) was conducted in the voltage window from 0.01 to 3.0 V vs. Li^+/Li. Figure 3a shows the first three CV curves of the electrode based on hollow $Mn_xFe_{3-x}O_4$ NPs at a scanning rate of 0.1 mV s^{-1}. During the first cycle, during lithiation, three cathodic peaks located at 1.62, 0.5, and 0.29 V were measured. The initial peak (1.62 V) was ascribed to the reduction of Fe^{3+} to Fe^{2+}. The other two cathodic peaks located at 0.5 and 0.29 V were assigned to the stepwise reduction of Fe^{2+} to Fe^0 and Mn^{2+} to Mn^0. In the subsequent anodic scan, corresponding to delithiation, two broad oxidation peaks at 1.68 V were assigned to the oxidation of Fe. No peaks at above 2.2 V were observed, which indicated that the further oxidation from Mn^{2+} to Mn^{3+} did not take place.

CV tests of electrodes based on Fe_3O_4 and Mn_5O_8 exhibited redox peaks in accordance with the above analysis (Figure S20). From these CV tests, it became evident that the peak

corresponding to the oxidation reaction of Mn to MnO had a low current density, what explained that this peak was not observed in the CV curve from the $Mn_xFe_{3-x}O_4$ electrode, as it was overlapped with the anodic peak of Fe oxidation.

After the first cycle, the reduction peaks associated with the lithiation process were merged to 0.74 V and their intensity decreased, which we associated to the formation of the solid-electrolyte interface (SEI) layer. The almost overlapped CV curves obtained for $Mn_xFe_{3-x}O_4$ electrodes in subsequent cycles indicated a high reversibility and excellent cycling stability for lithium storage. On the other hand, a serious fading process occurred on the Fe_3O_4 and Mn_5O_8 electrodes (Figure S20).

The initial galvanostatic discharge-charge profiles of $Mn_xFe_{3-x}O_4$ electrodes at a current density of 0.1 A g^{-1} are presented in Figure 3b. The discharge and charge capacities for the first cycle were 1522 and 1019 mAh g^{-1}, respectively, with a Coulombic efficiency of 67%. As expected, potential plateaus coincided with the distinct redox peaks in the CV curves measured from $Mn_xFe_{3-x}O_4$ electrodes. The initial capacity loss was ascribed to the formation of the SEI layer and the electrolyte decomposition. The overlapping of the following curves demonstrated the good reversibility of the reaction.

Charge-discharge tests at different current densities demonstrated $Mn_xFe_{3-x}O_4$ electrodes to deliver the best rate capabilities among the different electrode compositions tested (Figure 3c). $Mn_xFe_{3-x}O_4$, Fe_3O_4 and Mn_3O_4 electrodes displayed similar initial discharge capacities above 1350 mAh g^{-1}. However, a rapid capacity decay was obtained for Fe_3O_4 and Mn_3O_4 electrodes. For these electrodes, at high current densities of 5 A g^{-1}, no capacity was measured. The much higher capacity retention at high current densities of $Mn_xFe_{3-x}O_4$ electrodes was ascribed to a much faster electronic/ionic transport kinetics. Figure 3d shows the typical charge and discharge profiles of $Mn_xFe_{3-x}O_4$ electrodes at various current densities ranging from 0.1 to 5 A g^{-1}, showing average discharge capacities of 1054, 786, 685, 559, and 369 mAh g^{-1}, respectively. More importantly, when the current changed back to 0.1 A g^{-1}, a high discharge capacity of 960 mAh g^{-1} was still recovered for these electrodes, indicating the superior reversibility and stability of $Mn_xFe_{3-x}O_4$.

In terms of stability, $Mn_xFe_{3-x}O_4$ electrodes delivered a high capacity of 887 mAh g^{-1} at 0.3 A g^{-1} after 450 cycles. This represented a 118% capacity retention compared with the second discharge capacity. This result is in sharp contrast to that of Fe_3O_4 and Mn_3O_4 electrodes, which provided much lower capacities after 450 cycles, 458 and 265 mAh g^{-1}, respectively. At the high current density of 1 A g^{-1} (Figure S21), the capacity of $Mn_xFe_{3-x}O_4$ electrode was maintained at 361 mAh g^{-1} after 400 cycles, which is close to the theoretical capacity of

graphite (372 mAh g^{-1}). Table S1 provides a comparison of the capacity, rate capability, and cycling stability of LIB anodes based on Mn-Fe oxides, demonstrating the excellent performance of hollow $Mn_xFe_{3-x}O_4$ NP-based electrodes.

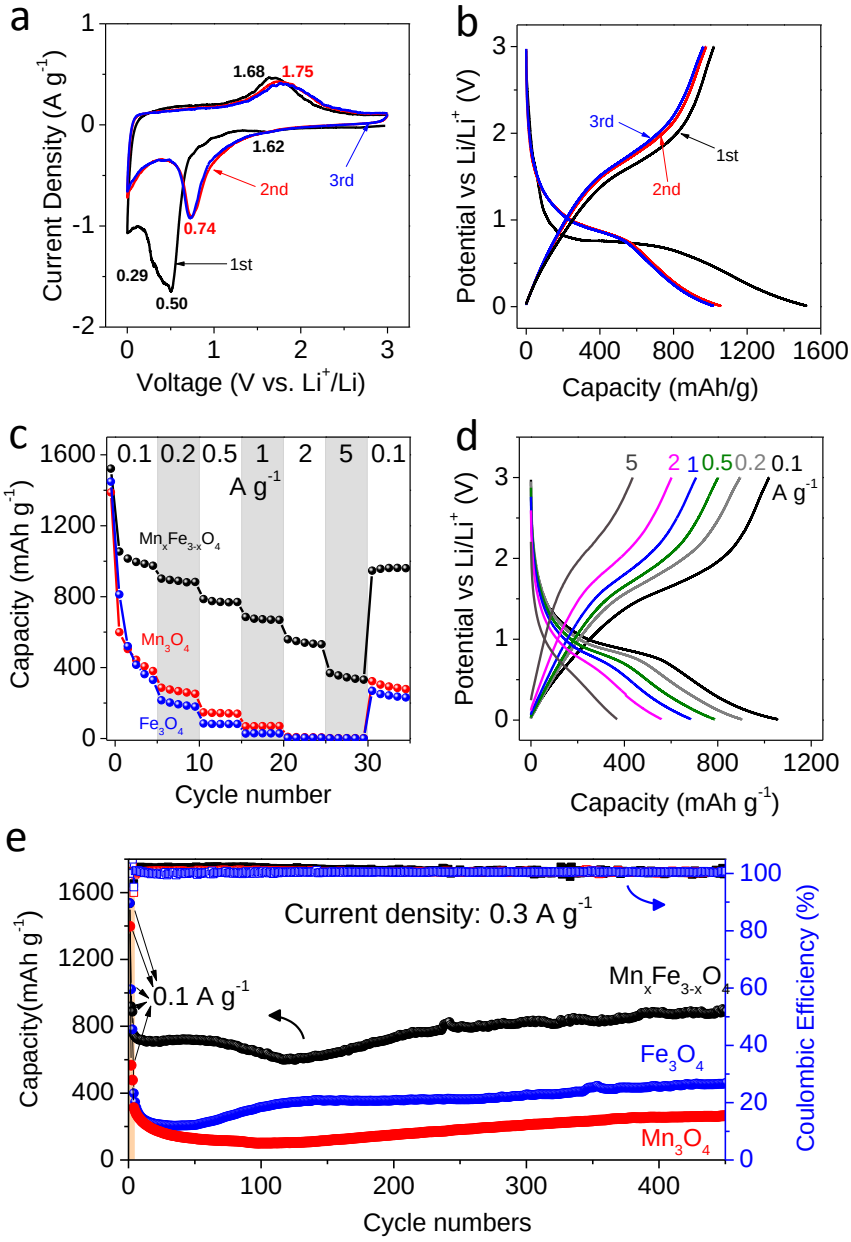

Figure 3. a) CV curves of a hollow $Mn_xFe_{3-x}O_4$-based electrode from 0.01 to 3.0 V at a scan rate of 0.2 mV s^{-1}. b) Charge/discharge curves of a $Mn_xFe_{3-x}O_4$-based electrode. c) Rate properties of $Mn_xFe_{3-x}O_4$, Fe_3O_4 and Mn_3O_4 electrodes at different current densities of 0.1, 0.2, 0.5, 1, 2, and 5 A g^{-1}. d) Charge/discharge curves of a $Mn_xFe_{3-x}O_4$-based electrode at different current densities. e) Long-term cycling performance of $Mn_xFe_{3-x}O_4$, Fe_3O_4 and Mn_3O_4 electrodes at a current density of 0.3 A g^{-1}. Electrodes were first activated at 0.1 A g^{-1} for 2 cycles.

EIS tests were carried out on $MnFe_2O_4$, Fe_3O_4 and Mn_3O_4 electrodes to investigate the kinetics of the process and the electrodes-electrolyte interaction (Figure 4). The Nyquist plot of the three fresh electrodes (Figure 4a) consisted of a semicircle in the high frequency range, associated to the charge-transfer resistance (R_{ct}) in the electrolyte−electrode interface and a straight line in the low frequencies, which was related to the Li^+ diffusion behavior in the electrode material. $MnFe_2O_4$ electrodes exhibited the smallest semicircle and sharpest straight line among the different electrodes tested. These results revealed the lowest R_{ct}, indicating a higher electrical conductivity that promoted electron transfer and favored of the further cycling test, and the fastest Li^+ diffusion in the electrode material, enhancing the rate performance. Figure 4b shows the Nyquist plots after cycling test. Compared with the fresh electrodes, the diameter of the semicircle of each electrode decreased, which we ascribed to the formation of a robust SEI layer during the cycling process. Compared with the other two electrode materials, the smallest semicircle at high frequencies and the steepest line at low frequencies obtained for the $Mn_xFe_{3-x}O_4$ electrodes, indicated the lowest R_{ct} and fastest Li^+ diffusion in these electrodes, which matched well with the highest reversible capacity obtained for this material during cycling. A more quantitative description of the EIS data obtained by modelling the electrical response with equivalent circuits (Figure 4c) confirmed the lower electrode (R_E) and especially charge transfer resistance (R_{ct}) of $Mn_xFe_{3-x}O_4$–based electrodes when compared with electrodes based on Fe_3O_4 and Mn_3O_4 (Table S2).[23-27]

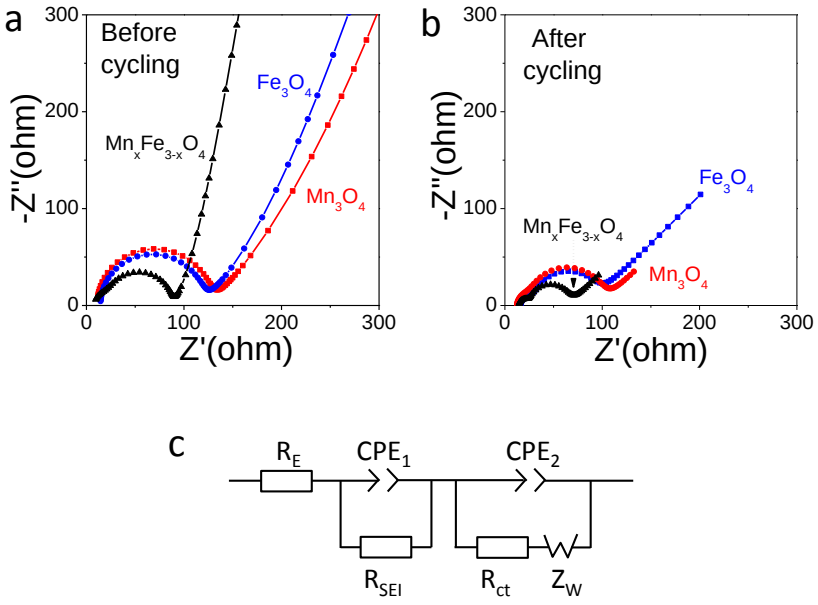

Figure 4. Nyquist plot of the impedance response of $Mn_xFe_{3-x}O_4$, Fe_3O_4 and Mn_3O_4 electrodes a) before and b) after cycling. c) Equivalent circuit used to fit the experimental data.

CONCLUSION

In summary, Fe_3O_4-Mn_5O_8 heterostructured NPs were synthesized using a simple seed-mediated growth method at low temperature using hollow Fe_3O_4 NPs as seeds. A low temperature (500 °C) annealing process was used to promote the solid state reaction between the two crystalline domains to produce hollow $Mn_xFe_{3-x}O_4$ NPs, thus conserving the original geometry. The same strategy could be applied to other mixed oxides to produce hollow NPs with multinary compositions from the low temperature solid state reaction of the constituent oxides pre-assembled to minimize the required ion diffusion distances into hollow heterostructures used as template. Hollow $Mn_xFe_{3-x}O_4$ NPs were used here as anode material in LIBs. Electrodes based on hollow $Mn_xFe_{3-x}O_4$ NPs displayed significantly improved LIBs performance over electrodes based on Fe_3O_4 and Mn_5O_8 NPs and over previously reported electrodes based on Mn-Fe oxides. $Mn_xFe_{3-x}O_4$ electrodes exhibited capacities up to 987.9 mA h g^{-1} at 0.1 A g^{-1} and 347.6 mA h g^{-1} at 5.0 A g^{-1}, with a complete recovery of the capacity after extensive cycling at various currents. We believe the polycrystalline shell, internal void space and higher surface area buffered the volume change and improved the stability of the hollow $Mn_xFe_{3-x}O_4$ NPs and consequently of the resulting LIBs.

AUTHOR INFORMATION

[1] X. Yu and C. Zhang contributed equally to this work.

Corresponding Authors

*E-mail: luozs@sustech.edu.cn (Z.L.).

*E-mail: acabot@irec.cat (A.C.).

AUTHOR CONTRIBUTIONS

This manuscript was prepared with the contribution of all the authors. A. Cabot and Z. Luo conceived the project, guided and supervised the work. X. Yu designed the experiments, produced all the materials and conducted the characterization including XRD, TEM and SEM-EDS, and wrote a first draft of the manuscript. C. Zhang performed all the electrochemical measurements, and the related data analysis and discussion. T. Zhang and J. Arbiol performed the structural and compositional characterization of the materials by means of HRTEM and EELS and discussed the results. J. Llorca conducted XPS measurement and analysis. J. Liu, J. Li, Y. Zuo significantly contributed to the experiments design, materials synthesis and characterization. J. J. Biendicho, and J. R. Morante provided valuable opinions

to the results discussion.

CONFLICTS OF INTERES

The authors declare no competing financial interest.

ACKNOWLEDGMENTS

This work was supported by the European Regional Development Funds and by the Spanish Ministerio de Economía y Competitividad through the project SEHTOP (ENE2016-77798-C4-3-R). X. Yu thanks the China Scholarship Council for the scholarship support. T. Zhang and J. Arbiol acknowledge funding from Generalitat de Catalunya 2017 SGR 327 and the Spanish MINECO coordinated projects between IREC and ICN2 VALPEC and subprojects RESOL and ANAPHASE (ENE2017-85087-C3). ICN2 acknowledges support from the Severo Ochoa Programme (MINECO, Grant no. SEV-2013-0295) and is funded by the CERCA Programme / Generalitat de Catalunya. J. Llorca is a Serra Húnter Fellow and is grateful to ICREA Academia program and to MINECO/FEDER grant ENE2015-63969-R and GC 2017 SGR 128.

REFERENCES

(1) Xie, Y.; Lou, X. W.; Yuan, C.; Wu, H. Bin; Xie, Y.; Wen, X.; Lou, D. Mixed Transition-Metal Oxides : Design , Synthesis , and Energy-Related Applications. *Angew. Chemie - Int. Ed.* **2014**, *53*, 1488–1504.

(2) Wu, F.; Bai, J.; Feng, J.; Xiong, S. Porous Mixed Metal Oxides: Design, Formation Mechanism , and Application in Lithium-Ion. *Nanoscale* **2015**, *7*, 17211–17230.

(3) Zhao, Q.; Yan, Z.; Chen, C.; Chen, J. Spinels : Controlled Preparation , Oxygen Reduction/Evolution Reaction Application , and Beyond. *Chem. Rev.* **2017**, *117*, 10121–10211.

(4) Xiao, Y.; Zai, J.; Tao, L.; Li, B.; Han, Q.; Yu, C.; Qian, X. $MnFe_2O_4$-Graphene Nanocomposites with Enhanced Performances as Anode Materials for Li-Ion Batteries. *Phys. Chem. Chem. Phys.* **2013**, *15*, 3939–3945.

(5) Lin, X.; Lv, X.; Wang, L.; Zhang, F.; Duan, L. Preparation and Characterization of $MnFe_2O_4$ in the Solvothermal Process : Their Magnetism and Electrochemical Properties. *Mater. Res. Bull.* **2013**, *48* (7), 2511–2516.

(6) Liu, Y.; Zhang, N.; Yu, C.; Jiao, L.; Chen, J. $MnFe_2O_4$@C Nanofibers as High-Performance Anode for Sodium-Ion Batteries. *Nano Lett.* **2016**, *16*, 3321–3328.

(7) Wang, B.; Chen, J. S.; Wu, H. Bin; Wang, Z. Quasiemulsion-Templated Formation of α-Fe_2O_3 Hollow Spheres with Enhanced Lithium Storage Properties. *J. Am. Chem. Soc.* **2011**, *133*, 17146–17148.

(8) Zhang, W. M.; Wu, X. L.; Hu, J. S.; Guo, Y. G.; Wan, L. J. Carbon Coated

Fe_3O_4nanospindles as a Superior Anode Material for Lithium-Ion Batteries. *Adv. Funct. Mater.* **2008**, *18* (24), 3941–3946.

(9) Zhang, L.; Wu, H. Bin; Lou, X. W. Iron-Oxide-Based Advanced Anode Materials for Lithium-Ion Batteries. *Adv. Energy Mater.* **2014**, *4* (4), 1–11.

(10) Wang, C.; Xu, C.; Zeng, H.; Sun, S. Recent Progress in Syntheses and Applications of Dumbbell-like Nanoparticles. *Adv. Mater.* **2009**, *21* (30), 3045–3052.

(11) Cabot, A.; Puntes, V. F.; Shevchenko, E.; Yin, Y.; Balcells, L.; Marcus, M. A.; Hughes, S. M.; Alivisatos, A. P. Vacancy Coalescence during Oxidation of Iron Nanoparticles. *J. Am. Chem. Soc.* **2007**, *129* (34), 10358–10360.

(12) Jiao, Y.; Han, D.; Liu, L.; Ji, L.; Guo, G.; Hu, J.; Yang, D.; Dong, A. Highly Ordered Mesoporous Few-Layer Graphene Frameworks Enabled by Fe_3O_4 nanocrystal Superlattices. *Angew. Chemie - Int. Ed.* **2015**, *54* (19), 5727–5731.

(13) Yu, H.; Guo, G.; Ji, L.; Li, H.; Yang, D.; Hu, J.; Dong, A. Designed Synthesis of Ordered Mesoporous Graphene Spheres from Colloidal Nanocrystals and Their Application as a Platform for High-Performance Lithium-Ion Battery Composite Electrodes. *Nano Res.* **2016**, *9* (12), 3757–3771.

(14) Hufschmid, R.; Arami, H.; Ferguson, R. M.; Gonzales, M.; Teeman, E.; Brush, L. N.; Browning, D.; Krishnan, K. M. Synthesis of Phase-Pure and Monodisperse Iron Oxide Nanoparticles by Thermal Decomposition. *Nanoscale* **2015**, *7*, 11142–11154.

(15) Luo, Z.; Irtem, E.; Ibánez, M.; Nafria, R.; MartÍ-Sánchez, S.; Genç, A.; De La Mata, M.; Liu, Y.; Cadavid, D.; Llorca, J.; et al. Mn_3O_4@$CoMn_2O_4$-Co_xO_y Nanoparticles: Partial Cation Exchange Synthesis and Electrocatalytic Properties toward the Oxygen Reduction and Evolution Reactions. *ACS Appl. Mater. Interfaces* **2016**, *8* (27), 17435–17444.

(16) Lee, K. S.; Anisur, R.; Kim, K. W.; Kim, W. S.; Park, T.; Kang, E. J.; Lee, I. S. Seed Size-Dependent Formation of Fe_3O_4/MnO Hybrid Nanocrystals: Selective, Magnetically Recyclable Catalyst Systems. *chem. Mater.* **2012**, *24*, 682–687.

(17) Li, S.; Shao, C.; Gu, W.; Rui, W.; Zhang, J.; Lai, J.; Li, H.; Ye, L. Targeted Imaging of Brain Gliomas Using. *RSC Adv.* **2015**, *5*, 33639–33645.

(18) Mayence, A.; Wéry, M.; Tran, D. T.; Wetterskog, E.; Svedlindh, P.; Tai, C. W.; Bergström, L. Interfacial Strain and Defects in Asymmetric Fe-Mn Oxide Hybrid Nanoparticles. *Nanoscale* **2016**, *8*, 14171–14177.

(19) Jiang, M.; Peng, X. Anisotropic Fe_3O_4/Mn_3O_4 Hybrid Nanocrystals with Unique Magnetic Properties. *Nano Lett.* **2017**, *17*, 3570–3575.

(20) Prabhu, R.; Sahu, B. N.; Venkataramani, N.; Prasad, S.; Krishnan, R. Magnetic Properties of Pulsed Laser Deposited $Co_{1-x}Zn_xFe_2O_4$ ($0.10 \leq x \leq 0.70$) Thin Films. *J. Magn. Magn. Mater.* **2018**, *448*, 192–198.

(21) You, A.; Be, M. A. Y.; In, I. Effect of Substrate Temperature on Magnetic Properties of $MnFe_2O_4$ Thin Films. *AIP Adv.* **2018**, *8*, 056112.

(22) Anerjee, D. B. Interpretation of XPS Mn (2p) Spectra of Mn Oxyhydroxides and Constraints on the Mechanism of MnO_2 Precipitation. *Am. Mineral.* **1998**, *83*, 305–315.

(23) Shi, Y.; Chou, S.; Wang, J.; Li, H.; Liu, H.; Wu, Y. In-Situ Hydrothermal Synthesis of

Graphene Woven VO_2 Nanoribbons with Improved Cycling Performance. *J. Power Sources* **2013**, *244*, 684–689.

(24) Min, J.; Na, Y.; Lee, J.; Chan, Y. Electrochimica Acta Superior Electrochemical Properties of Rutile VO_2-Carbon Composite Microspheres as a Promising Anode Material for Lithium Ion Batteries. *Electrochim. Acta* **2015**, *156*, 179–187.

(25) Wang, X.; Chen, K.; Wang, G.; Liu, X.; Wang, H. Rational Design of Three-Dimensional Graphene Encapsulated with Hollow FeP@Carbon Nanocomposite as Outstanding Anode Material for Lithium Ion and Sodium Ion Batteries. *ACS Nano* **2017**, *11*, 11602–11616.

(26) Guo, W.; Wang, Y.; Li, Q.; Wang, D.; Zhang, F.; Yang, Y.; Yu, Y. SnO_2@C@VO_2 Composite Hollow Nanospheres as an Anode Material for Lithium-Ion Batteries. *ACS Appl. Mater. Interfaces* **2018**, *10*, 14993–15000.

(27) Tian, W.; Hu, H.; Wang, Y.; Li, P.; Liu, J.; Liu, J.; Wang, X.; Xu, X.; Li, Z.; Zhao, Q.; et al. Metal−Organic Frameworks Mediated Synthesis of One-Dimensional Molybdenum-Based/Carbon Composites for Enhanced Lithium Storage. *ACS Nano* **2018**, *12*, 1990–2000.